Journal of Materials Chemistry A

PAPER

View Article Online
View Journal | View Issue

Cite this: J. Mater. Chem. A, 2019, 7, 18488

Two-step growth of $CsPbI_{3-x}Br_x$ films employing dynamic CsBr treatment: toward all-inorganic perovskite photovoltaics with enhanced stability†

Bhaskar Parida,[a] Jun Ryu,[a] Saemon Yoon,[a] Seojun Lee,[a] Yejin Seo,[a] Jung Sang Cho[b] and Dong-Won Kang *[a]

Received 4th June 2019
Accepted 17th July 2019

DOI: 10.1039/c9ta05948b

rsc.li/materials-a

Recently, $CsPbI_{3-x}Br_x$ (x = 1–2) all-inorganic perovskites have been studied to overcome the phase instability of $CsPbI_3$. However, the addition of Br inevitably leads to a bandgap that is too wide (1.93–2.03 eV) compared to that of $CsPbI_3$ (1.73 eV). To avoid this, the present study focuses on developing stable α-$CsPbI_{3-x}Br_x$ (x < 0.7) perovskite films with lower Br levels. Our dynamic CsBr treatment incorporates Br^- into the $CsPbI_3$ lattice, greatly enhancing the morphology, optical properties, stability, and photovoltaic performance of the resultant $CsPbI_{3-x}Br_x$ (x < 0.7) perovskite films. At x = 0.66, the perovskite film with the relatively low bandgap of 1.84 eV contributes to achieving an impressive power conversion efficiency (PCE) of 14.08% and, after 1200 h storage under a nitrogen atmosphere without encapsulation, the PCE remains at around 70% of this initial level. This two-step growth using dynamic CsBr treatment opens up promising routes for the feasible fabrication of inorganic perovskite photovoltaics with exceptional stability.

1. Introduction

Recently, all-inorganic perovskites such as cesium-based metal halide perovskites ($CsMX_3$, where M = Pb or Sn; X = Cl, Br, or I) have drawn considerable research interest because of their excellent thermal stability and optoelectronic properties compared to organic–inorganic hybrid perovskites (*i.e.* methylammonium lead triiodide, $MAPbI_3$), which means that they hold great promise for use in perovskite solar cells, tandem solar cells, and other optoelectronic devices.[1–6] Typically, $CsPbI_3$ inorganic perovskites exhibit a bandgap of E_g = 1.73 eV, which makes them particularly suitable for solar energy conversion.[7] The black cubic phase of $CsPbI_3$ (α-$CsPbI_3$) can be obtained by heating yellow-phase (with an orthorhombic non-perovskite structure, *i.e.*, δ-$CsPbI_3$) perovskite film at high temperatures over 300 °C.[8] However, α-$CsPbI_3$ is unstable under ambient conditions because of its low tolerance factor (t) just above 0.8, and the small Cs cation cannot hold the PbI_6 octahedral frame in the cubic perovskite structure. Thus, the α-$CsPbI_3$ rapidly transits to δ-$CsPbI_3$, which is stable at ambient room temperature but cannot absorb sufficient sunlight in the visible and long-wavelength regions because of its high bandgap (E_g = 2.8 eV).[1,9] Therefore, significant efforts have been made to overcome the instability issues in $CsPbI_3$ inorganic PSCs, including the addition of hydrogen iodide,[1] sulfobetaine zwitterion,[10] ethylenediamine,[11] phenylethylammonium iodide (PEAI),[12] $HPbI_3$,[13] BiI_3,[14] CaI,[15] H_2O,[16] or polyvinyl pyridine (PVP)[17] to the precursor solution, reducing the crystal size,[18] or introducing intermediate phases such as Cs_4PbI_6.[19] To date, the highest recorded power conversion efficiency (PCE) of 17.06% and the excellent photostability of $CsPbI_3$ inorganic PSCs has been achieved with simple post-treatment with a phenyltrimethylammonium bromide (PTABr) solution.[20] Despite the high performance of these PSCs, their stability significantly deteriorates in an ambient atmosphere.

The partial incorporation of Br into $CsPbI_3$ has been found to be very useful for stabilizing the cubic phase of $CsPbI_3$ in an ambient atmosphere.[21] Therefore, CsBr-rich $CsPbI_{3-x}Br_x$ perovskites have been reported.[22] In particular, $CsPbI_2Br$ and $CsPbIBr_2$ inorganic perovskites have been widely investigated because these show high moisture stability.[21,22] However, the stability and E_g of these perovskites increase as the Br content increases, which narrows the light-harvesting range and limits their PCE. Wang *et al.* reported a solvent control growth approach for a stoichiometric solution process to fabricate $CsPbI_{3-x}Br_x$ inorganic perovskite solar cells that generated a high PCE of 16.14%.[23] However, these PSCs were only stable in an inert atmosphere. Similarly, Li *et al.* reported a non-stoichiometric solution process that introduced CsBr to a $CsPbI_3$ perovskite precursor solution to fabricate stable α-phase $CsPbI_3$ or $CsPbI_{3-x}Br_x$ films.[24] However, the CsBr had

[a]School of Energy Systems Engineering, Chung-Ang University, Seoul 06974, Republic of Korea. E-mail: kangdwn@cau.ac.kr; Tel: +82-2-820-5414

[b]Department of Engineering Chemistry, Chungbuk National University, 28644, Republic of Korea

† Electronic supplementary information (ESI) available. See DOI: 10.1039/c9ta05948b

lower grain size and more microstrain-driven pinholes, which limited the PCE to an average of 10.12%. In addition, Yu *et al.* developed solvent engineering with two-step multiple spin-coating to fabricate $CsPb(I_xBr_{1-x})_3$ films for stable high-performance inorganic PSCs.[25] However, the bandgap of the $CsPb(I_xBr_{1-x})_3$ inorganic perovskite film ($E_g = 2.03$ eV) was close to that of $CsPbIBr_2$ ($E_g = 2.05$ eV), which prevents sufficient light absorption. Therefore, fabricating efficient and stable inorganic perovskites with suitable bandgaps for inorganic perovskite and tandem solar cells remains a challenge.

The present paper reports $CsPbI_{3-x}Br_x$ ($x < 0.7$) perovskites processed by introducing a simple and novel two-step method. We first prepared α-phase $CsPbI_3$ perovskite films by drying $CsPbI_3$ perovskite films at room temperature and then dynamically spin-cast a CsBr precursor onto the α-phase $CsPbI_3$ followed by drying at 100 °C and subsequent annealing at 300 °C. We found that a small fraction of the Br^- from the CsBr was sufficient to enhance the quality of the perovskite crystals and phase stability in ambient air compared to previous reports.[24,25] Notably, desired changes in the absorption band edge and a tunable E_g (1.84 eV), which was much lower than that of $CsPbI_2Br$ (1.93 eV), was made possible by varying the CsBr concentration. Thus, high-quality $CsPbI_{3-x}Br_x$ ($x < 0.7$) perovskite films were obtained with optimal CsBr concentrations ($x = 0.66$), contributing to an excellent PCE of 14.08% (open-circuit voltage [V_{oc}] of 1.12 V; short circuit current [J_{sc}] of 16.36 mA cm^2; fill factor [FF] of 76.87%). Additionally, 97% and 70% of the initial PCE was still possible after 60 h and 1200 h of storage under ambient conditions without any encapsulation, representing exceptional stability compared to control $CsPbI_3$ and previous studies.[14,24] The proposed two-step process based on the dynamic drop-casting of a small amount of CsBr on a $CsPbI_3$ film not only improves the surface morphology and crystallinity but also reduces the grain boundary trap densities of the mixed halide all-inorganic perovskites. In addition, the developed perovskites demonstrated outstanding device performance and stability, thus demonstrating significant potential as the technical foundation for further progress in the development of inorganic perovskite photovoltaics.

2. Experimental section

2.1 Materials preparation

The materials used in this study were purchased from commercial sources and used as received. Lead iodide (PbI_2, 99.9985%), cesium iodide (CsI), CsBr, SnO_2 (15 wt% in an H_2O colloidal dispersion), poly(3-hexylthiophene-2,5-diyl) (P3HT), and LiCl were purchased from Alfa Aesar. *N*,*N*-Dimethylformamide (DMF; 99%) and dimethyl sulfoxide (DMSO; 99.9%) were purchased from Samchun Chemicals, and chlorobenzene (99.8%) was purchased from Kanto Chemical. The $CsPbI_3$ perovskite precursor solution was prepared by dissolving an equimolar ratio of PbI_2 (0.8 M) and CsI (0.8 M) in a mixed solvent of (4 : 1) DMF : DMSO. The precursor solution was magnetically stirred overnight at 60 °C and the CsBr solutions were prepared by dissolving 5, 10, or 15 mg of CsBr in methanol. Note that a concentration of CsBr greater than 15 mg was found to be insoluble in methanol at room temperature (see Fig. S1 in the ESI†). Therefore, we prepared a CsBr/methanol solution with a maximum of 15 mg of CsBr per 1 mL of methanol. A hole transport layer (HTL) was created by dissolving 10 mg of P3HT in 1 mL of chlorobenzene and stirring the solution overnight at room temperature. The P3HT solution was filtered before use. SnO_2 was used as an electron transport layer (ETL) and was prepared as described in a previous report.[26] Briefly, the SnO_2 precursor solution was prepared by dissolving an SnO_2 (450 μL) colloid dispersion and an LiCl (300 μL) aqueous solution (17 mg/4 mL) in 1.7 mL of deionized water (DI) water while stirring at room temperature for four hours.

2.2 Solar cell fabrication and characterization

Planar inorganic PSCs were fabricated with a device structure of ITO/SnO_2/$CsPbI_3$ or ITO/SnO_2/$CsPbI_{3-x}Br_x$/P3HT/Au. First, ITO substrates with a resistance of 15 Ω sq^{-1} were sequentially cleaned using a detergent solution, DI water, acetone, and isopropanol (IPA) for 15 min each. After cleaning and drying, the substrates were treated with ozone (O_3) plasma for 20 min to increase their surface wettability. The ETL was obtained by spin-coating an SnO_2 precursor onto the ITO substrates at 4000 rpm for 30 s in ambient air and annealing for 170 °C for 30 min. After cooling to room temperature, the substrates were transferred to a nitrogen-filled glovebox with air and H_2O content >1 ppm for coating with the $CsPbI_3$ perovskite layer. The $CsPbI_3$ perovskite solution was filtered with a PVDF (0.45 μM) filter, spin-coated onto the SnO_2 layer at 2000 rpm for 45 s, and then dried for 50 min at room temperature. Following this, 100 μL of the CsBr solutions of various concentrations were dynamically spin-coated onto the $CsPbI_3$ film at 3000 rpm for 30 s and dried at 100 °C for 5 min. A reference sample without CsBr treatment was annealed at 340 °C for 8 min and the CsBr-coated samples were annealed at 300 °C for 8 min. Fig. 1 shows the experimental process used to fabricate $CsPbI_{3-x}Br_x$ inorganic perovskite films. The HTL layer was spin-coated onto $CsPbI_3$ and $CsPbI_{3-x}Br_x$ at 1500 rpm for 30 s and dried at 85 °C for 5 min. Finally, 100 nm of Au electrodes were deposited on top of the devices using a thermal evaporator at 1.2×10^{-6} Torr after defining an effective cell area of 0.04 cm^2 with a shadow mask. Note that the $CsPbI_{3-x}Br_x$ perovskite films with various dynamic CsBr treatments – 0, 5, 10, or 15 mg – are referred to as CsBr-0, CsBr-5, CsBr-10, and CsBr-15, respectively, for the remainder of the paper.

All characterizations were carried out in an ambient atmosphere. The structural properties of the perovskite films were characterized using X-ray diffraction (XRD; R&D-100; Rigaku SmartLab). The surface and cross-sectional morphologies and the elemental mapping of the prepared films and devices were investigated using a field-emission scanning electron microscope (FE-SEM; SIGMA, Carl Zeiss). The absorption spectra of the planar perovskite films were characterized by ultraviolet-visible (UV-vis) spectrophotometry (UV-2700; Shimadzu). Steady-state PL measurements of the fabricated perovskite films were conducted using a spectrofluorometer (FP-8600, Jasco) with a laser excitation wavelength of 405 nm. All current–voltage

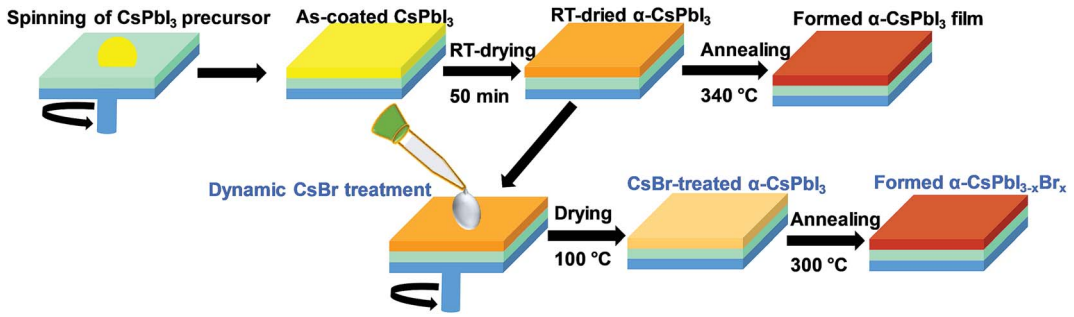

Fig. 1 Schematic preparation process for α-$CsPbI_3$ and α-$CsPbI_{3-x}Br_x$ inorganic perovskite films without and with a dynamic coating of a CsBr/methanol solution of various concentrations.

(*J*–*V*) curves and the steady-state photocurrent of the fabricated PVSCs were measured using a solar simulator (PEC-L01, Peccell Technologies) under standard AM1.5 illumination (100 mW cm^{-2}) in atmospheric air conditions. The external quantum efficiency (EQE) spectrum was measured using a power source (Abet Technologies 150 W xenon lamp, 13014) with a monochromator (DongWoo Optron, MonoRa500i) and a CompactStat (Ivium Technologies; Eindhoven, The Netherlands) to detect responses as a function of the spectral wavelengths. Electrochemical impedance spectroscopy (EIS) measurements were carried out using an impedance analyzer (Solartron 1287) under AM1.5 illumination with an applied bias of 0.8 V for frequencies in the range 1–200 kHz.

3. Results and discussion

We prepared the $CsPbI_3$ inorganic perovskite films using a simple spin-coating and drying process at room temperature, with the $CsPbI_3$ precursor prepared by dissolving an equimolar ratio of PbI_2 and CsI in a mixture of DMF and DMSO. Fig. S2 in the ESI† presents the fabrication process for $CsPbI_3$ perovskite films with and without CsBr treatment. The spin-coated $CsPbI_3$ perovskite films on glass were greenish-yellow in color, as shown in Fig. S2(a).† After 50 min of drying, the $CsPbI_3$ perovskite film turned brown, as shown in Fig. S2(b),† indicating the formation of α-phase $CsPbI_3$ film, as previously reported.[23] The high boiling point (189 °C) and low vapor pressure (126 Pa at 25 °C) of DMSO reduces the solvent evaporation rate of as-coated $CsPbI_3$ perovskite and forms DMSO residuals, which enhance the nucleation and crystal growth of the perovskite. Therefore, the δ-phase of the $CsPbI_3$ perovskite film (as spin-coated) changed into α-phase after 50 min of drying at room temperature (Fig. S2(b)†). The room-temperature drying process improved the morphology of the $CsPbI_3$ film and as a result produced high-quality black α-phase $CsPbI_3$ perovskite film after annealing, as shown in Fig. S2(c).† To fabricate $CsPbI_{3-x}Br_x$ perovskite film, we dynamically drop-casted a CsBr precursor of various concentrations on the room-temperature-dried α-phase $CsPbI_3$ films (Fig. S2(d)†). In addition, we used the dropping and spin-coating of CsBr solution on room-temperature-dried α-$CsPbI_3$ films to produce $CsPbI_{3-x}Br_x$ perovskite films. However, the dropping of the CsBr solution resulted in the formation of circles on the $CsPbI_3$ perovskite film, indicating deterioration of the film (Fig. S3†). Interestingly, the dynamic drop-casting of the CsBr solution with concentrations of 5, 10, and 15 mg was found to produce uniform and damage-free CsBr-treated $CsPbI_3$ film (Fig. S2(e)–(g)†). After dynamic CsBr treatment and drying at 100 °C, the $CsPbI_3$ film turned yellow and light brown for the perovskite films coated with CsBr-5, 10, and 15 mg (Fig. S2(e)–(g)†). This indicates that the dynamic coating of CsBr with a concentration of 10 or 15 mg maintained the α-phase of the $CsPbI_3$ perovskite film. High-quality $CsPbI_{3-x}Br_x$ perovskite films with CsBr-5, -10, and -15 treatment were obtained after the samples were annealed at 300 °C (Fig. S2(i)–(k)†). Notably, the CsBr-coated $CsPbI_3$ perovskite films transformed into the yellow δ-phase when the temperature increased from RT to 270 °C and the black α-phase was gradually observed above 250 °C for CsBr-15. The annealing temperature of 300 °C was sufficient to obtain high-quality $CsPbI_{3-x}Br_x$ perovskite films. However, the $CsPbI_3$ film without CsBr coating could not be converted to the black α-phase at 300 °C (Shown in Fig. S2(h)†).

Fig. 2(a) shows the XRD patterns of the δ-$CsPbI_3$ and the α-phase $CsPbI_{3-x}Br_x$ perovskite films. The XRD patterns of the δ-$CsPbI_3$ were located at $2\theta = 13.16°$, 22.78°, and 26.57°, which are indexed to the (012), (112), and (122) planes, respectively. These peaks disappeared after annealing the δ-$CsPbI_3$ perovskite film, while peaks at 14.42°, 20.80°, and 29.02° appeared, indexing to the (100), (110), and (200) planes, respectively, which indicated the formation of pure α-phase $CsPbI_3$ perovskite film. The peak positions were in good agreement with previous research.[10,23] As the CsBr concentration increased from 5 mg to 15 mg, the intensity of the (100) and (200) peaks gradually increased. Interestingly, the diffraction peak intensity of the CsBr-15 film that corresponded to the (100) peak was five times higher than that of the CsBr-0 film. These results suggest that the additional dynamic coating of CsBr on $CsPbI_3$ enhances the crystallinity and reduces grain boundary scattering and intragranular defects.[22,27] In addition, the high intensity of the (100) peaks in all of the inorganic perovskite films suggests that the perovskite grains possess a preferable (100) orientation. Perovskite grains with a (100) orientation are postulated to be perpendicular to the SnO_2/ITO substrate, which can be highly beneficial for carrier transportation and injection in solar cells.[28,29]

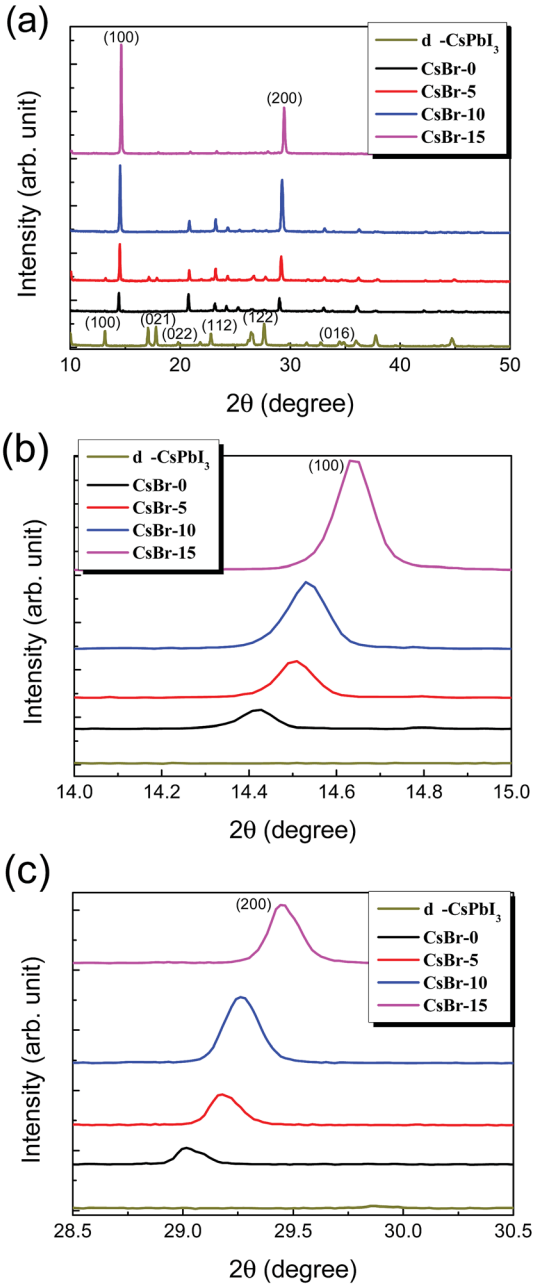

Fig. 2 (a) XRD patterns of the α-$CsPbI_{3-x}Br_x$ inorganic perovskite films with CsBr concentrations (0, 5, 10, and 15 mg). The magnified XRD patterns in the region of (b) 14–15° and (c) 28.5–30.5° for the corresponding (100) and (200) planes of the film. The magnified XRD patterns show that the shift of the peaks towards higher angles increased with increasing CsBr concentration.

With an increase in the CsBr concentration from CsBr-0 to CsBr-15, the (100) peaks of the perovskite films clearly shifted from 14.42° to 14.50°, 14.53°, and 14.63° (shown in Fig. 3(b)), and the (200) peaks shifted from 29.01° to 29.18°, 29.26, and 29.44° (shown in Fig. 3(c)) respectively. Because we measured our films (without encapsulation) under atmospheric air conditions, the α-$CsPbI_3$ and the CsBr-5 perovskite films were found to be slightly degraded. Therefore, some orthorhombic δ-

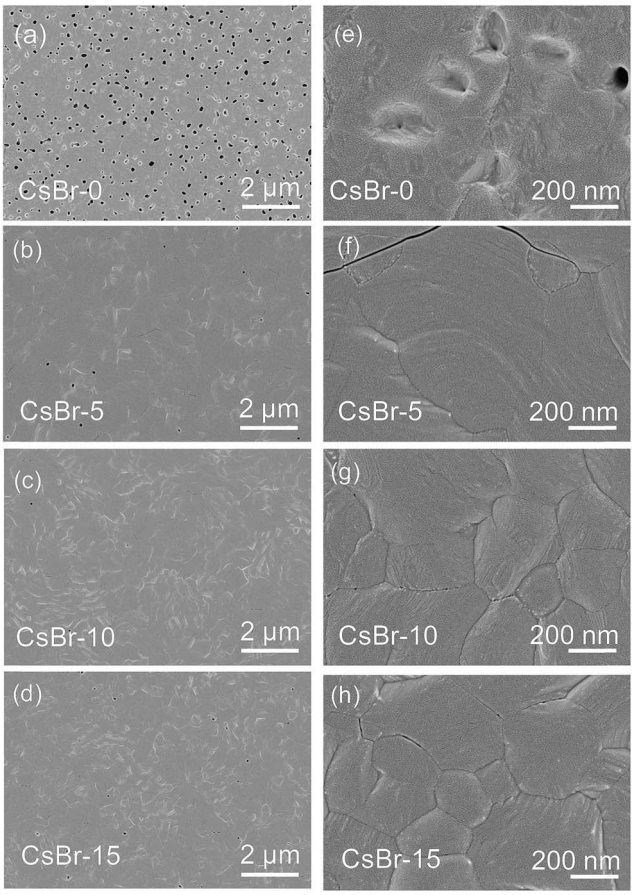

Fig. 3 Top-view FE-SEM images of the $CsPbI_{3-x}Br_x$ inorganic perovskite films without and with a dynamic coating of CsBr with concentrations of (a) 0, (b) 5, (c) 10, and (d) 15 mg; corresponding magnified images are shown in (e–h), respectively.

$CsPbI_3$ perovskite peaks appeared in the XRD patterns. This indicates that CsBr-5 film is not able to improve the phase stability of the $CsPbI_3$ perovskites. Previous research has reported that the incorporation of one Br^- atom into each lattice of $CsPbI_3$ results in the formation of $CsPbI_2Br$ perovskites with (100) and (200) planes located at $2\theta = 14.9°$ and 29.8°, respectively.[22] This indicates that the (100) and (200) peak positions of α-$CsPbI_3$ perovskites are lower than the peak positions of $CsPbI_2Br$. When our CsBr treatment was carried out on the α-$CsPbI_3$ perovskite films and annealed, the Br atoms were partially incorporated into the α-$CsPbI_3$, resulting in the peak shifting towards a higher angle, which is similar to a previous report.[24] However, the (100) and (200) peaks of our perovskite film exhibited a lower angle than that of the (100) and (200) peaks of $CsPbI_2Br$. This indicates that the additional CsBr dynamic coating resulted in the formation of perovskite films with Br/I ratios less than 0.5, which is the ratio in $CsPbI_2Br$. This indicates that our perovskite films exhibit a stoichiometry of $CsPbI_{3-x}Br_x$ ($x < 1$).

The surface morphology of $CsPbI_{3-x}Br_x$ perovskite films with different CsBr treatments (CsBr-0, CsBr-5, CsBr-10, and CsBr-15) was analyzed using top-view FE-SEM images, as shown in

Fig. 3(a)–(d), respectively. The control $CsPbI_3$ film (CsBr-0) exhibited many pinholes with poor surface coverage and a rough surface (Fig. 3(a) and (e)). With CsBr-5 treatment, the surface morphology was significantly improved, with fewer pinholes (Fig. 3(b)). However, grain boundary cracks were observed, as shown in Fig. 3(f). Notably, a very smooth surface with few pinholes was observed for the CsBr-10 and CsBr-15 films, though tiny pinholes at the grain boundary were observed (Fig. 3(c) and (d)), which may be linked to the micro-strain in the crystal lattice caused by CsBr.[28] Interestingly, the grain boundaries of the CsBr-15 film were better than those of the CsBr-0, CsBr-5 and CsBr-10 films (Fig. 3(h)). The elimination of pinholes and grain boundary cracks suggests that the dynamic CsBr treatment approach has a significant positive effect on grain growth, uniformity, and coverage. The average grain size of the CsBr-0 film was found to be 300–500 nm, which increased by over 2 μm in the CsBr-15 film using the dynamic casting method (Fig. S4†), which is consistent with the XRD results. This indicates that the additional CsBr coating followed by the annealing process increased the grain size and significantly reduced the grain boundary. Furthermore, the grain sizes were found to exceed the thickness of the perovskite film (410 nm) after CsBr coating and annealing. The reduction in the grain boundary can enhance carrier lifetime by removing surface trap states, enhancing the transport of photo-generated carriers along the vertical direction in the perovskite absorber, and protecting the crystal from moisture penetration through the grain boundary.[30,31]

It has been reported that room-temperature-dried $CsPbI_3$ perovskite film exhibits DMSO residuals, which enhances the mass transportation and diffusion and thus improves perovskite film quality.[23] Specifically, the DMSO molecules interact with PbI_2 to form DMSO-coordinated PbI_2 arrays consisting of layered octahedral $[PbI_6]^{4-}$ and expand the interlayer distance of PbI_2 along the *c*-axis.[32] At the same time, CsI species in the precursor film are easily inserted into the lattice of PbI_2 to form a large amount of CsI–PbI_2–DMSO intermediate phases, which are beneficial for large crystal grain size and a smooth surface morphology. Because CsI has a higher affinity for PbI_2 than DMSO, an intermolecular exchange occurs between CsI species and DMSO molecules, which results in the formation of dark-brown α-phase $CsPbI_3$ perovskite films at room temperature (shown in the photographic image in Fig. S2(d)†).[33] When CsBr was coated on room-temperature-dried $CsPbI_3$ film, the DMSO coordinated with PbI_2 could be washed out because of the negligible solubility of PbI_2 in methanol.[25] Thus, when the CsBr/methanol solution comes in contact with the PbI_2, nucleation occurs due to the partial diffusion of CsBr into the PbI_2 even after the coating and drying process (without the high-temperature annealing). This phenomenon was confirmed by the change in the color (from dark brown to light brown) of the perovskite film in CsBr-10 and CsBr-15. Moreover, the slight addition of Br can inhibit the back-conversion of the cubic phase into yellow non-perovskite phase and stabilizes the perovskite film,[34] which has been confirmed by the drying of the $CsPbI_{3-x}Br_x$ films after CsBr coating and drying at 100 °C, as the films maintained the cubic phase. Finally, when annealing the films at 300 °C, more Br atoms were diffused into the films with simultaneous nucleation and grain growth resulting in the formation of a more desirable smooth cubic $CsPbI_{3-x}Br_x$ film with large grains.

The UV-vis absorption spectra and the PL spectra of the perovskite films according to dynamic CsBr treatment are shown in Fig. 4(a) and (b), respectively. CsBr-0 ($CsPbI_3$) film exhibited an absorption band edge at 710 nm, corresponding to a bandgap of 1.75 eV, which is in good agreement with a previous report.[35] By increasing the CsBr concentration from CsBr-5 to CsBr-15, the band edges exhibited a blueshift from 692 nm to 672 nm. As a result, the corresponding bandgaps of the perovskite films increased from 1.79 eV to 1.84 eV from CsBr-5 to CsBr-15. A similar trend in the PL peaks shifting to shorter wavelengths was also observed with increasing CsBr concentration. The peak shifts in both absorbance and PL results are associated with the substitution of I^- by the smaller-radius Br^-.[24] Consequently, it is noted that the bandgap of our CsBr-15 film (1.84 eV) was still lower than that of $CsPbI_2Br$ (1.93 eV).[21] We further observed that the PL peak intensities of the $CsPbI_{3-x}Br_x$ perovskite films were higher than those of the CsBr-0 film, which suggests that the additional dynamic coating of CsBr significantly reduced the non-radiative recombination rate within the perovskite films. Notably, the presence of the highest PL peak in the CsBr-15 film indicates that the crystal defects related to grain boundaries and halide deficiencies were

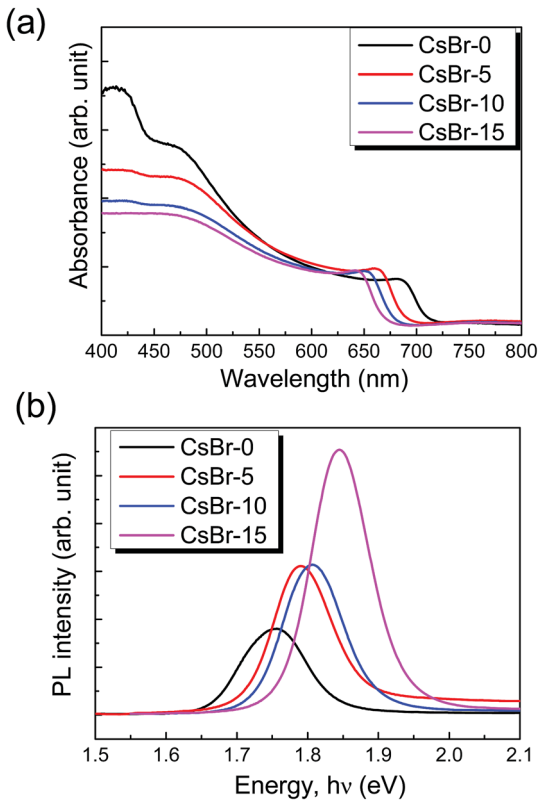

Fig. 4 (a) UV-vis absorption spectra and (b) steady-state PL spectra for the $CsPbI_{3-x}Br_x$ inorganic perovskite films prepared without and with a dynamic coating of CsBr of various concentrations.

significantly lower, which is speculated to promote its phase stability.[33] Moreover, the blueshift in the PL peaks indicates that the trap densities near the band edge of the film are lowered by the introduction of Br. Thus, a low recombination loss and high photo-carrier collection in the film can be expected.

The linear trend in the bandgap changes indicates that the perovskite films consisted of a mixture of iodide and bromide. To verify this hypothesis, we conducted EDX measurements for the elemental analysis of the perovskite films. The EDX spectra of the control CsBr-0 are shown in Fig. S5(a),† and the CsBr-5, CsBr-10, and CsBr-15 films are shown in Fig. S5(b), (c), and (d),† respectively. The quantified atomic ratio of the films is shown in Table 1. The Si, O, and C peaks were observed from the EDX spectra that arose from the substrate and carbon tape, respectively. Similarly, the Pt spectra arose due to the Pt coating on the samples. Br atoms were absent in CsBr-0 film because CsBr treatment was not applied. Notably, Br atoms gradually increased in number with increasing CsBr concentration. Therefore, these results confirm that our dynamic CsBr-treated $CsPbI_3$ perovskite films consisted of a $CsPbI_{3-x}Br_x$ stoichiometry that was formed due to the partial substitution of I by Br atoms due to the CsBr dynamic coating. From the atomic ratio of I and Br, we determined the stoichiometry of the films to be $CsPbI_{2.64}Br_{0.36}$, $CsPbI_{2.48}Br_{0.52}$, and $CsPbI_{2.34}Br_{0.66}$ for the CsBr-5, CsBr-10, and CsBr-15 films, respectively. The increase in Br atoms in the films increased the bandgap, from which it can be expected that the V_{oc} of the PSCs may increase. To further verify the distribution of the Br atoms in the perovskite grains, cross-sectional EDX mapping of the CsBr-15 film was carried out, as shown in Fig. S6.† The mapping results clearly indicate that the Br atoms are uniformly distributed within the film, with negligible differences in elemental distribution. All other elements were also uniformly distributed.

To investigate the effect of CsBr treatment on the performance of the PSCs, we fabricated $CsPbI_{3-x}Br_x$-based solar cells with the planar architecture of ITO/SnO_2/$CsPbI_{3-x}Br_x$/P3HT/Au (Fig. 5(a)). A cross-sectional FE-SEM image of the $CsPbI_{3-x}Br_x$ perovskite solar cell is presented in Fig. 5(b), showing an SnO_2 (30 nm) ETL layer on an ITO glass substrate, a 410 nm-thick perovskite layer, and a P3HT (200 nm) HTL layer. The *J–V* curves of the $CsPbI_{3-x}Br_x$ PSCs are shown in Fig. 5(c) and their photovoltaic parameters are summarized in Table 2. The CsBr-0 device produced a PCE of 8.40% with a V_{oc} of 0.88 V, a J_{sc} of 17.20 mA cm^{-2}, and an FF of 56.47%. The performance of the $CsPbI_{3-x}Br_x$ PSCs gradually increased with increasing CsBr concentration from CsBr-5 to CsBr-15 due to the increase in V_{oc} and FF. Thus, the notable increase in V_{oc} and FF of the $CsPbI_{3-x}Br_x$ devices can be attributed to two factors: (i) the increase in the bandgap with increasing the CsBr concentration and (ii) the reduction in grain boundary trap densities by CsBr,[28,36] which was confirmed by the absorption band edge and PL spectra, respectively. For the $CsPbI_{2.34}Br_{0.66}$ (CsBr-15) PSC, device performance was very high, with a PCE of 14.08%, a V_{oc} of 1.12 V, a J_{sc} of 16.36 mA cm^{-2}, and an FF of 76.87%, which is higher than previous reports.[24,25] For J_{sc}, the $CsPbI_{3-x}Br_x$ devices had lower values than that of the control CsBr-0 device, indicating that the CsBr-coated devices showed a trade-off relation between the band gap and J_{sc}. From the results, CsBr-15 was the optimal treatment, significantly reducing grain boundary-related recombination, resulting in higher V_{oc}, FF, J_{sc}, and device performance. Regarding situations of much Br introduction, we verified the $CsPbI_{3-x}Br_x$ device performance by increasing the CsBr concentration of 20 mg. Due to the solubility limit of CsBr (maximum of 15 mg) in methanol as discussed above, significant efforts have been made to prepare CsBr methanol solution (20 mg mL^{-1}) and finally we could obtain the solution by applying heating (at 50 °C) the solution. After that we applied the CsBr-20 to fabricate 2-step processed $CsPbI_{3-x}Br_x$ perovskite films and its application to photovoltaic device. As indicated in Fig. S7,† we observed the PCE and J_{sc} of the CsBr-20 device as 11.61% and 14.58 mA cm^{-2}, respectively. The above result indicates that the PCE drops due to the decrease of J_{sc} by increasing the Br content in the $CsPbI_{3-x}Br_x$ perovskite. Thus, we could present more clearly that CsBr-15 is the optimal condition in this work in order to achieve high PCE of 14.08% for the $CsPbI_{3-x}Br_x$ perovskite base solar cells.

In contrast, a device with CsBr-0 film suffered from surface recombination due to the presence of many pinholes and the degradation to the δ-phase during air measurements, which resulted in a low PCE. Furthermore, the $CsPbI_{3-x}Br_x$-based planar devices exhibited *J–V* hysteresis in both the forward and reverse scanning directions (Fig. S8, and Table S1†). The hysteresis is probably due to the light-induced iodide and bromide phase segregation in the mixed halide compositions, which has been unavoidable in most of the inorganic PSCs to date.[37] It has been reported that the mixed halide inorganic perovskites under illumination form iodide-rich $CsPbI_{(1+x)}$-$Br_{(2-x)}$ phases at the grain boundaries which segregate as clusters in the film. This phase segregation generates a high density of mobile ions which accumulate at the perovskite/carrier transport layer interface and hampers the carrier extraction and lead to the formation of a robust *J–V* hysteresis in the perovskite solar cells.[37] However, the hysteresis behavior in the mixed halide inorganic perovskite solar cells can be reduced by more improved compositional engineering and new techniques which can minimize the mobile ions by reducing the density of ionic vacancies.[22,38] Furthermore, the hysteresis can be eliminated by interfacial engineering, such as interface passivation, surface passivation, and the use of highly conducting carrier transport layers to suppress the ionic accumulation and efficiently extract the carriers.[19,28,39,40]

It is also speculated that the remaining small *J–V* hysteresis may not a severe problem if stabilized power output (SPO) shows stable performance, because practical solar modules

Table 1 The quantified atomic ratio for the α-$CsPbI_{3-x}Br_x$ perovskite films as obtained from EDX measurements

Elements (at%)	CsBr-0	CsBr-5	CsBr-10	CsBr-15
Cs	9.92	10.44	10.22	11.02
Pb	9.20	9.79	9.88	10.54
I	31.27	27.98	26.42	27.83
Br	0	3.82	5.49	7.91

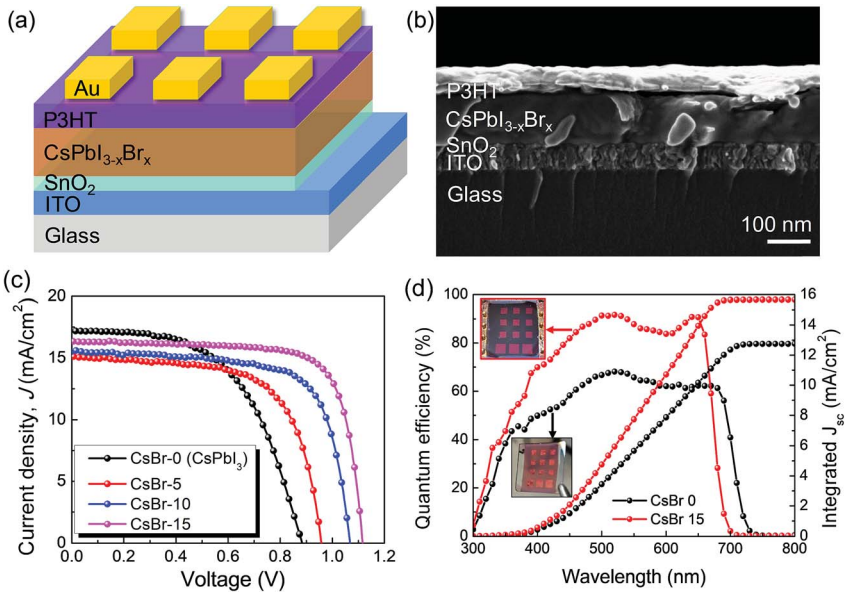

Fig. 5 (a) Schematic diagram and (b) cross-sectional FE-SEM image of $CsPbI_{3-x}Br_x$ inorganic PSCs. (c) *J–V* characteristic curves for the $CsPbI_{3-x}Br_x$ inorganic PSCs fabricated without and with a dynamic coating of CsBr of various concentrations. (d) IPCE of the control CsBr-0 and optimal CsBr-15 solar cells with their corresponding integrated J_{sc} curves. The insets with black and red borders show the degraded control CsBr-0 and highly stable CsBr-15 solar cells after IPCE measurements in air.

operate under maximum power point tracking (MPPT) rather than forward/reverse scan modes. Hence, we have also investigated SPO of our $CsPbI_{3-x}Br_x$ inorganic perovskite solar cells, as shown in Fig. S9.† The stabilized photocurrent and PCE of the CsBr-0 (Fig. S9(a)†) and CsBr-15 (Fig. S9(b)†) were measured by holding their bias of 0.66 V and 0.93 V near maximum power point under AM1.5 illumination, respectively. We obtained a stabilized photocurrent of 10.31 mA cm^{-2} and 14.00 mA cm^{-2}, corresponding to a stabilized PCE of 6.80% and 13.02% for the CsBr-0 and CsBr-15 PSCs, respectively. The photocurrent density and PCE of the unencapsulated CsBr-0 ($CsPbI_3$) device could not be stable because of its continuous degradation in the humid ambient of atmospheric air. It is noteworthy that the SPO of the devices were measured in air ambient without device encapsulation under high relative humidity (R.H.) of 50–60%. Nevertheless, the CsBr-15 PSC revealed remarkably stable operation and good PCE over 13%, which suggests significantly enhanced stability from our dynamic CsBr treatment technique for inorganic PSCs. It should also be noted that the average device performance was also collected from 20 devices, which are shown in Table 2. In addition, Fig. S10† shows a distribution of PCE of these 20 devices for (a) CsBr 0, (b) CsBr 5, (c) CsBr 10 and (d) CsBr 15 solar cells. The average PCE value of 13.41% for the devices with CsBr-15 film indicates the high reproducibility of our approach of coating CsBr on $CsPbI_3$ perovskites to improve their stability and performance. This high reproducibility can be partly attributed to the growth of high-quality perovskite crystals with reduced grain boundaries using the optimal CsBr coating and diffusion process.

The external quantum efficiency (EQE) spectrum of the $CsPbI_3$ (CsBr-0) and the $CsPbI_{2.34}Br_{0.66}$ (CsBr-15) devices are shown in Fig. 5(d). Both devices produced EQE spectra from the entire wavelength range (300–720 nm and 300–700 nm, respectively), which is consistent with the absorption spectra. However, the CsBr-0 device contributed over 60% of the photon-to-current conversion at wavelengths ranging from 450 to 680 nm, while the CsBr-15 device contributed over 80% for the same wavelength range. Similarly, the integrated photocurrent densities of the control CsBr-0 and CsBr-15 film-based devices were 12.69 and 15.69 mA cm^{-2}, respectively. The main reason

Table 2 Performance of the $CsPbI_{3-x}Br_x$ perovskite solar cells fabricated without and with a dynamic coating of CsBr

Samples	Direction	PCE (%)	V_{oc} (V)	J_{sc} (mA cm^{-2})	FF (%)
CsBr-0	Average	7.41 ± 1.01	0.87 ± 0.71	15.47 ± 1.56	54.78 ± 6.72
	Champion	8.40	0.88	17.20	56.47
CsBr-5	Average	8.16 ± 0.86	0.90 ± 0.05	14.92 ± 1.11	60.98 ± 5.04
	Champion	9.63	0.96	15.23	66.02
CsBr-10	Average	10.78 ± 0.65	1.05 ± 0.02	14.78 ± 0.62	69.51 ± 5.52
	Champion	11.81	1.06	15.54	71.33
CsBr-15	Average	13.41 ± 0.51	1.10 ± 0.04	15.84 ± 0.52	76.78 ± 2.21
	Champion	14.08	1.12	16.36	76.87

for the low EQE and integrated J_{sc} of the control CsBr-0 film-based device was that the device degraded during the measurement of EQE in ambient air, as illustrated in the image with a black border in the inset of Fig. 5(d). On the other hand, the CsBr-15 film-based device was highly stable in ambient air without any encapsulation while measuring EQE, as shown in the red-bordered inset of Fig. 5(d), which significantly contributed to the photon-to-current conversion efficiency. The integrated J_{sc} of the CsBr-15 film-based device was in fairly good agreement with the J_{sc} obtained from J–V measurements.

In order to understand the significant differences in the photovoltaic properties of the CsBr-0 and CsBr-15 film-based devices, we compared their dark J–V curves (Fig. 6(a)). The devices with CsBr-15 film exhibited a higher onset voltage than the control device with CsBr-0 film in the linear-scale dark J–V curve, indicating the formation of a stronger depleted electric field in $SnO_2/CsPbI_{2.34}Br_{0.66}$, which contributes to improving the V_{oc}.[33,41] Furthermore, the $CsPbI_{2.34}Br_{0.66}$ (CsBr-15) device exhibited a leakage current one-order lower than that of the control device, as shown in the semi-log J–V curve in Fig. 6(b). The low leakage current is highly beneficial to the improvement in the V_{oc} of a cell,[42] which is consistent with the J–V results for the CsBr-coated devices.

To fully delineate the charge carrier transportation and recombination dynamics of our inorganic PSCs, we carried out EIS measurements. Fig. 6(c) presents the Nyquist plots of the control CsBr-0 ($CsPbI_3$) and CsBr-15 devices with an applied bias of 0.8 V under simulated AM1.5 illumination. The results were fitted to the equivalent circuit (EC) diagram, as shown in the inset of Fig. 6(c). The EC consists of the sheet resistance (R_s) and charge transport resistance (R_{ct}), which are summarized in Table 3. The R_s values can be obtained from the starting point of the Nyquist plot. The R_s values of the cells were almost same because the ETL and HTL layers were the same in all of the devices. However, the R_{ct} (obtained from the diameter of the semicircle in the Nyquist plot) of the CsBr-15 device (464.82 Ω) was significantly lower than that of the control device with CsBr-0 film (799.94 Ω). This indicates that the charge transport resistance of the CsBr-treated device was lower, which can be ascribed to the pure cubic phase and the high surface coverage with large grain sizes. The low capacitance of the CsBr-15 device further indicates that carrier accumulation at the grain boundaries and the interfaces was reduced, resulting in the high extraction of charge carriers. Thus, we can conclude that CsBr treatment plays a vital role in reducing the grain-boundary-related trap densities and enhancing the carrier transport between the perovskite and carrier transport layers. As a result, V_{oc} and FF were higher. In addition, the high resistance in the control CsBr-0 device was possibly caused by the δ-phase[14] due to its rapid degradation in ambient air, resulting in its poor performance.

Table 3 Parameters employed for the fitting of the impedance spectra using an equivalent circuit diagram

Samples	R_s (Ω cm^2)	R_{ct} (Ω cm^2)	C (F cm^{-2})
CsBr-0	26.12	799.94	5.75×10^{-9}
CsBr-15	25.48	464.82	2.12×10^{-9}

We also determined the carrier relaxation time from the frequency-dependent imaginary parts of the impedance of the control CsBr-0 and CsBr-15 devices. The frequency-dependent

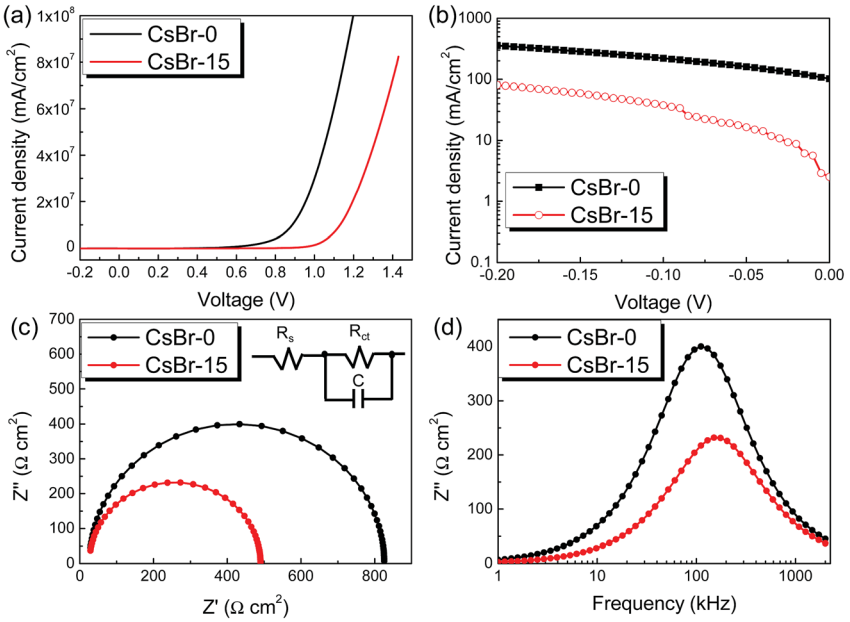

Fig. 6 (a) Linear and (b) semi-log J–V curves of the control CsBr-0 and CsBr-15 solar cells measured in dark conditions. (c) Nyquist plots of the control CsBr-0 and CsBr-15 solar cells obtained from impedance spectroscopy measurements. The spectra were measured under AM1.5 illumination with a bias of 0.8 V. The inset shows the equivalent circuit diagram used for fitting. (d) Frequency-dependent imaginary parts of the impedance spectra of the control CsBr-0 and CsBr-15 solar cells.

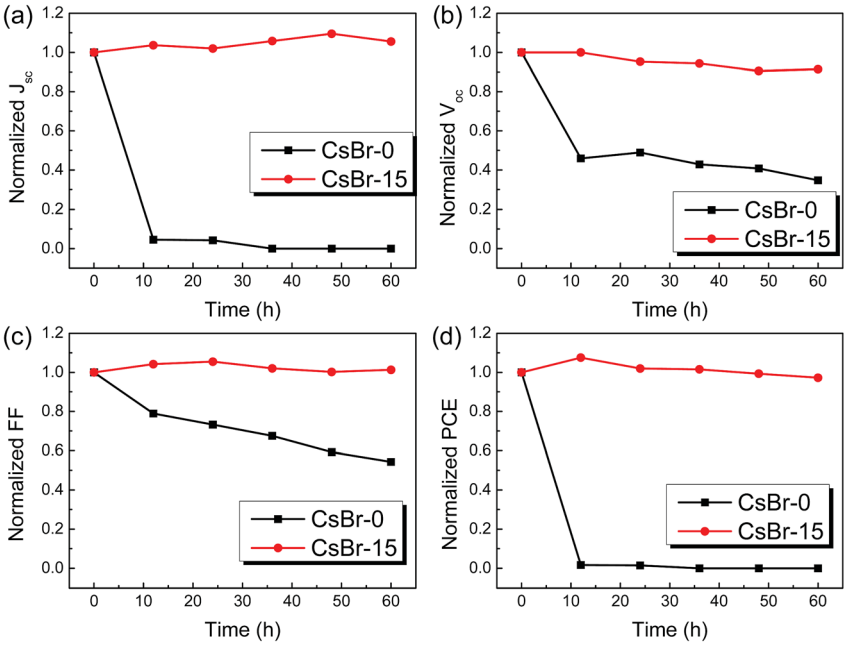

Fig. 7 Normalized (a) J_{sc}, (b) V_{oc}, (c) FF, and (d) PCE as a function of time for the control CsBr-0 and CsBr-15 solar cells without encapsulation. Note that all measurements were carried out in air-ambient, and the devices were kept in a nitrogen-filled glovebox.

imaginary parts of impedance, which are usually used to calculate the relaxation frequency of the most resistive contribution, are shown in Fig. 6(d). It can be seen that the center of the characteristic frequency (f_{max}) of the device with CsBr-15 film shifted to a higher frequency (150.92 kHz) compared to the peak (111.93 kHz) of the control CsBr-0 device. It is well-known that the relaxation time (τ) is inversely proportional to f_{max}, *i.e.*, $\tau \propto 1/f_{max}$, so the τ value of the CsBr-15 device is smaller than that of CsBr-0, indicating the faster charging and discharging of carriers at the interface.[43] Consequently, the smaller τ suggests that charge transportation is enhanced in the CsBr-15 active layer, significantly improving the V_{oc} and FF.

Finally, we tested the stability of the unencapsulated perovskite solar cells with CsBr-0 and CsBr-15 films in dark conditions in a nitrogen-filled glovebox. Note that, for the device stability test, we stored the devices in the glovebox and performed the measurements in ambient air each time. Fig. 7(a)–(d) show the normalized J_{sc}, V_{oc}, FF, and PCE of the devices as a function of time, respectively. It can be seen that the device with CsBr-15 perovskite maintained a PCE that was over 97% of the initial PCE after 60 h. However, the control device with CsBr-0 film was already degraded after the initial PCE measurement. Thus, the PSC with CsBr-15 film showed excellent stability compared to the control device with CsBr-0 film. In addition, the unencapsulated CsBr-15 PSC retained a PCE that was about 70% of the initial PCE after storage for over 1200 h in a nitrogen filled glove box (Fig. S11†), which is much better than previous reports.[14,24] We have also tested the stability of our $CsPbI_{3-x}Br_x$ ($x < 0.7$) perovskite devices (without encapsulation) under ambient air at the elevated temperature of 85 °C and relative humidity (R.H.) of 40% for accelerated degradation tests, as shown in below Fig. S12(a)–(d).† For comparison, recent reports regarding stability for inorganic PSCs are also summarized in Table S2.† We observed that during the first 24 h the J_{sc} and FF were increased, which contributed to enhance the PCE due to the oxidation of P3HT in air.[44] The PCE, J_{sc} and FF were stable and the initial PCE showed almost no degradation after 48 h despite continuous heating at 85 °C in air, which indicates that our dynamic CsBr treatment can significantly enhance the stability of $CsPbI_3$, because pristine device (CsBr-0) was quickly degraded within 1 h. When we compare this result with previous work[18] in terms of identical duration (testing for 48 h) from above Table S2,† our device showed pronounced stability although our tests have been carried out at 85 °C that is much higher than their condition (25 °C).

On the basis of those experimental results, we can conclude that a small amount of Br from the additional dynamic treatment with CsBr can significantly enhance device performance, stability, and reproducibility.

4. Conclusions

In summary, we developed a simple two-step approach for the dynamic CsBr treatment of $CsPbI_3$ perovskite film to fabricate highly stable α-$CsPbI_{3-x}Br_x$ ($x < 0.7$) perovskite films with lower Br levels. The CsBr played a vital role in the formation of pure and high-quality α-$CsPbI_3$ perovskites, the presence of which were confirmed by XRD patterns and EDX mapping. The UV-vis absorption and PL spectra further confirmed that the bandgap of the $CsPbI_3$ inorganic perovskites changed with increasing CsBr concentration due to the incorporation of a small amount of Br^- into the $CsPbI_3$ lattice. The α-$CsPbI_{3-x}Br_x$ perovskite films possessed a much more suitable bandgap (1.84 eV) compared with that of $CsPbI_2Br$ (1.93 eV) with the optimal CsBr-

15 treatment. The solar cell fabricated with the CsBr-15 treatment exhibited an impressive PCE of 14.08% and demonstrated excellent stability, holding the PCE at 70% of its initial levels during storage for over 1200 h in N_2 atmosphere without encapsulation. This indicates that CsBr treatment enhanced the phase stability of the $CsPbI_3$ perovskite films, allowing the films and devices to be characterized in ambient air, unlike recently reported $CsPbI_3$ and/or $CsPbI_2Br$ devices, which are typically measured in a nitrogen-filled atmosphere due to their rapid phase degradation. Therefore, our work suggests that the dynamic CsBr treatment is highly beneficial for stabilizing α-$CsPbI_3$ perovskites, and this process can thus be implemented in the development of highly efficient industrial-scale inorganic perovskite and tandem solar cells.

Conflicts of interest

There are no conflicts of interest to declare.

Acknowledgements

This work was supported by the National Research Foundation of Korea (NRF) grant funded by the Korea government (MSIT) (NRF-2018R1C1B6008028 and 2018R1A4A1024691).

References

1 G. E. Eperon, G. M. Paternò, R. J. Sutton, A. Zampetti, A. A. Haghighirad, F. Cacialli and H. J. Snaith, *J. Mater. Chem. A*, 2015, **3**, 19688–19695.
2 Y. Wang, X. Li, J. Song, L. Xiao, H. Zeng and H. Sun, *Adv. Mater.*, 2015, **27**, 7101–7108.
3 L. Protesescu, S. Yakunin, M. I. Bodnarchuk, F. Krieg, R. Caputo, C. H. Hendon, R. X. Yang, A. Walsh and M. V. Kovalenko, *Nano Lett.*, 2015, **15**, 3692–3696.
4 Y. Li, Z. Shi, L. Lei, F. Zhang, Z. Ma, D. Wu, T. Xu, Y. Tian, Y. Zhang, G. Du, C. Shan and X. Li, *Chem. Mater.*, 2018, **30**, 6744–6755.
5 N. Yantara, S. Bhaumik, F. Yan, D. Sabba, H. A. Dewi, N. Mathews, P. P. Boix, H. V. Demir and S. Mhaisalkar, *J. Phys. Chem. Lett.*, 2015, **6**, 4360–4364.
6 P. Luo, W. Xia, S. Zhou, L. Sun, J. Cheng, C. Xu and Y. Lu, *J. Phys. Chem. Lett.*, 2016, **7**, 3603–3608.
7 R. E. Beal, D. J. Slotcavage, T. Leijtens, A. R. Bowring, R. A. Belisle, W. H. Nguyen, G. F. Burkhard, E. T. Hoke and M. D. McGehee, *J. Phys. Chem. Lett.*, 2016, **7**, 746–751.
8 J. K. Nam, D. H. Chun, R. J. K. Rhee, J. H. Lee and J. H. Park, *Adv. Sci.*, 2018, **5**, 1800509.
9 C.-Y. Chen, H.-Y. Lin, K.-M. Chiang, W.-L. Tsai, Y.-C. Huang, C.-S. Tsao and H.-W. Lin, *Adv. Mater.*, 2017, **29**, 1605290.
10 Q. Wang, X. Zheng, Y. Deng, J. Zhao, Z. Chen and J. Huang, *Joule*, 2017, **1**, 371–382.
11 T. Zhang, M. I. Dar, G. Li, F. Xu, N. Guo, M. Grätzel and Y. Zhao, *Sci. Adv.*, 2017, **3**, e1700841.
12 Y. Wang, T. Zhang, M. Kan, Y. Li, T. Wang and Y. Zhao, *Joule*, 2018, **2**, 2065–2075.
13 S. Xiang, Z. Fu, W. Li, Y. Wei, J. Liu, H. Liu, L. Zhu, R. Zhang and H. Chen, *ACS Energy Lett.*, 2018, **3**, 1824–1831.
14 Y. Hu, F. Bai, X. Liu, Q. Ji, X. Miao, T. Qiu and S. Zhang, *ACS Energy Lett.*, 2017, **2**, 2219–2227.
15 C. F. J. Lau, X. Deng, J. Zheng, J. Kim, Z. Zhang, M. Zhang, J. Bing, B. Wilkinson, L. Hu, R. Patterson, S. Huang and A. Ho-Baillie, *J. Mater. Chem. A*, 2018, **6**, 5580–5586.
16 B. Zhao, S.-F. Jin, S. Huang, N. Liu, J.-Y. Ma, D.-J. Xue, Q. Han, J. Ding, Q.-Q. Ge, Y. Feng and J.-S. Hu, *J. Am. Chem. Soc.*, 2018, **140**, 11716–11725.
17 B. Li, Y. Zhang, L. Fu, T. Yu, S. Zhou, L. Zhang and L. Yin, *Nat. Commun.*, 2018, **9**, 1076.
18 A. Swarnkar, A. R. Marshall, E. M. Sanehira, B. D. Chernomordik, D. T. Moore, J. A. Christians, T. Chakrabarti and J. M. Luther, *Science*, 2016, **354**, 92.
19 L. A. Frolova, Q. Chang, S. Y. Luchkin, D. Zhao, A. F. Akbulatov, N. N. Dremova, A. V. Ivanov, E. E. M. Chia, K. J. Stevenson and P. A. Troshin, *J. Mater. Chem. C*, 2019, **7**, 5314–5323.
20 Y. Wang, T. Zhang, M. Kan and Y. Zhao, *J. Am. Chem. Soc.*, 2018, **140**, 12345–12348.
21 R. J. Sutton, G. E. Eperon, L. Miranda, E. S. Parrott, B. A. Kamino, J. B. Patel, M. T. Hörantner, M. B. Johnston, A. A. Haghighirad, D. T. Moore and H. J. Snaith, *Adv. Energy Mater.*, 2016, **6**, 1502458.
22 C. F. J. Lau, X. Deng, Q. Ma, J. Zheng, J. S. Yun, M. A. Green, S. Huang and A. W. Y. Ho-Baillie, *ACS Energy Lett.*, 2016, **1**, 573–577.
23 P. Wang, X. Zhang, Y. Zhou, Q. Jiang, Q. Ye, Z. Chu, X. Li, X. Yang, Z. Yin and J. You, *Nat. Commun.*, 2018, **9**, 2225.
24 Z. Li, J. Xu, S. Zhou, B. Zhang, X. Liu, S. Dai and J. Yao, *ACS Appl. Mater. Interfaces*, 2018, **10**, 38183–38192.
25 B. Yu, H. Zhang, J. Wu, Y. Li, H. Li, Y. Li, J. Shi, H. Wu, D. Li, Y. Luo and Q. Meng, *J. Mater. Chem. A*, 2018, **6**, 19810–19816.
26 J. Wei, F. Guo, X. Wang, K. Xu, M. Lei, Y. Liang, Y. Zhao and D. Xu, *Adv. Mater.*, 2018, **30**, 1805153.
27 W. Zhu, C. Bao, B. Lv, F. Li, Y. Yi, Y. Wang, J. Yang, X. Wang, T. Yu and Z. Zou, *J. Mater. Chem. A*, 2016, **4**, 12535–12542.
28 C. Liu, W. Li, C. Zhang, Y. Ma, J. Fan and Y. Mai, *J. Am. Chem. Soc.*, 2018, **140**, 3825–3828.
29 J. Lin, M. Lai, L. Dou, C. S. Kley, H. Chen, F. Peng, J. Sun, D. Lu, S. A. Hawks, C. Xie, F. Cui, A. P. Alivisatos, D. T. Limmer and P. Yang, *Nat. Mater.*, 2018, **17**, 261–267.
30 Z. Zeng, J. Zhang, X. Gan, H. Sun, M. Shang, D. Hou, C. Lu, R. Chen, Y. Zhu and L. Han, *Adv. Energy Mater.*, 2018, **8**, 1801050.
31 F. Wang, S. Bai, W. Tress, A. Hagfeldt and F. Gao, *npj Flexible Electron.*, 2018, **2**, 22.
32 N. J. Jeon, J. H. Noh, Y. C. Kim, W. S. Yang, S. Ryu and S. I. Seok, *Nat. Mater.*, 2014, **13**, 897.
33 W. Zhu, Q. Zhang, D. Chen, Z. Zhang, Z. Lin, J. Chang, J. Zhang, C. Zhang and Y. Hao, *Adv. Energy Mater.*, 2018, **8**, 1802080.
34 W. S. Yang, J. H. Noh, N. J. Jeon, Y. C. Kim, S. Ryu, J. Seo and S. I. Seok, *Science*, 2015, **348**, 1234.
35 Y. Fu, M. T. Rea, J. Chen, D. J. Morrow, M. P. Hautzinger, Y. Zhao, D. Pan, L. H. Manger, J. C. Wright,

R. H. Goldsmith and S. Jin, *Chem. Mater.*, 2017, **29**, 8385–8394.
36 G. Yin, H. Zhao, H. Jiang, S. Yuan, T. Niu, K. Zhao, Z. Liu and S. Liu, *Adv. Funct. Mater.*, 2018, **28**, 1803269.
37 W. Li, M. U. Rothmann, A. Liu, Z. Wang, Y. Zhang, A. R. Pascoe, J. Lu, L. Jiang, Y. Chen, F. Huang, Y. Peng, Q. Bao, J. Etheridge, U. Bach and Y.-B. Cheng, *Adv. Energy Mater.*, 2017, **7**, 1700946.
38 H. Zai, D. Zhang, L. Li, C. Zhu, S. Ma, Y. Zhao, Z. Zhao, C. Chen, H. Zhou, Y. Li and Q. Chen, *J. Mater. Chem. A*, 2018, **6**, 23602–23609.
39 L. Yan, Q. Xue, M. Liu, Z. Zhu, J. Tian, Z. Li, Z. Chen, Z. Chen, H. Yan, H.-L. Yip and Y. Cao, *Adv. Mater.*, 2018, **30**, 1802509.
40 D. Wei, F. Ma, R. Wang, S. Dou, P. Cui, H. Huang, J. Ji, E. Jia, X. Jia, S. Sajid, A. M. Elseman, L. Chu, Y. Li, B. Jiang, J. Qiao, Y. Yuan and M. Li, *Adv. Mater.*, 2018, **30**, 1707583.
41 L. Zhu, J. Shi, S. Lv, Y. Yang, X. Xu, Y. Xu, J. Xiao, H. Wu, Y. Luo, D. Li and Q. Meng, *Nano Energy*, 2015, **15**, 540–548.
42 F. Zhang, J. Song, L. Zhang, F. Niu, Y. Hao, P. Zeng, H. Niu, J. Huang and J. Lian, *J. Mater. Chem. A*, 2016, **4**, 8554–8561.
43 B. Parida, A. Singh, M. Oh, M. Jeon, J.-W. Kang and H. Kim, *Mater. Today Commun.*, 2019, **18**, 176–183.
44 D. C. J. Neo, N. Zhang, Y. Tazawa, H. Jiang, G. M. Hughes, C. R. M. Grovenor, H. E. Assender and A. A. R. Watt, *ACS Appl. Mater. Interfaces*, 2016, **8**, 12101–12108.